

SMA observations of the W3(OH) complex: Dynamical differentiation between W3(H₂O) and W3(OH)

Sheng-Li Qin,^{1*} Peter Schilke,² Jingwen Wu,³ Tie Liu,⁴ Yuefang Wu,⁵
 Álvaro Sánchez-Monge² and Ying Liu⁶

¹Department of Astronomy, Yunnan University, and Key Laboratory of Astroparticle Physics of Yunnan Province, Kunming 650091, China

²I. Physikalisches Institut, Universität zu Köln, Zùlpicher Str. 77, D-50937 Köln, Germany

³Department of Physics and Astronomy, University of California, Los Angeles, CA 90095, USA

⁴Korea Astronomy and Space Science Institute 776, Daedeokdaero, Yuseong-gu, Daejeon 305-348, Republic of Korea

⁵Department of Astronomy, Peking University, Beijing 100871, China

⁶Department of Physics and Hebei Advanced Thin Film Laboratory, Hebei Normal University, Shijiazhuang 050024, China

Accepted 2015 November 26. Received 2015 November 25; in original form 2015 August 30

ABSTRACT

We present Submillimeter Array observations of the HCN (3–2) and HCO⁺ (3–2) molecular lines towards the W3(H₂O) and W3(OH) star-forming complexes. Infall and outflow motions in the W3(H₂O) have been characterized by observing HCN and HCO⁺ transitions. High-velocity blue/red-shifted emission, tracing the outflow, show multiple knots, which might originate in episodic and precessing outflows. ‘Blue-peaked’ line profiles indicate that gas is infalling on to the W3(H₂O) dust core. The measured large mass accretion rate, $2.3 \times 10^{-3} M_{\odot} \text{ yr}^{-1}$, together with the small free-fall time-scale, $5 \times 10^3 \text{ yr}$, suggest W3(H₂O) is in an early evolutionary stage of the process of formation of high-mass stars. For the W3(OH), a two-layer model fit to the HCN and HCO⁺ spectral lines and *Spitzer*/Infrared Array Camera (IRAC) images support that the W3(OH) H II region is expanding and interacting with the ambient gas, with the shocked neutral gas being expanding with an expansion time-scale of $6.4 \times 10^3 \text{ yr}$. The observations suggest different kinematical time-scales and dynamical states for the W3(H₂O) and W3(OH).

Key words: stars: formation – ISM: individual objects: W3(H₂O) – ISM: individual objects: W3(OH) – ISM: kinematics and dynamics.

1 INTRODUCTION

Current theories and observations suggest that low-mass stars form by gravitational collapse and subsequent accretion through a circumstellar disc, with the accretion energy driving a collimated outflow perpendicular to the plane of the disc (Shu, Adams & Lizano 1987). Therefore, accretion discs and outflows are physically connected and are key ingredients in the process of formation of low-mass stars. For high-mass stars, their formation process is still not well understood. Outflows are frequently detected in high-mass star-forming regions, but it is thought that high-mass star formation is not merely a scaled-up version of the low-mass star formation process characterized by larger outflow parameters (e.g. Wu et al. 2004), poor collimation around massive young stars (e.g. Shepherd & Churchwell 1996; Zhang et al. 2005) and higher accretion rates (see review by Zinnecker & Yorke 2007). Additionally, discs in high-mass young stellar objects are still elusive – only a few of them have been detected (Zhang, Hunter & Sridharan 1998;

Shepherd, Claussen & Kurtz 2001; Jiang et al. 2005; Patel et al. 2005; Sánchez-Monge et al. 2013a, 2014) – probably due to their short lifetimes, the necessity of achieving high angular resolution (not available in the observations prior to Atacama Large Millimeter Array) and source confusion in dense clusters. Therefore, the study and characterization of the outflow and infall processes involved in the formation of high-mass stars need to be understood in more detail. Since high-mass stars form in dense cores, dense gas tracers such as HCN are useful in identifying outflow and infall motions (e.g. Wu et al. 2005; Liu et al. 2011a,b, 2013, 2015). It has also been demonstrated that the profile of spectral lines such as HCN (3–2) and HCO⁺ (3–2) are good tools to search for and study the infall motions (see simulations by Smith et al. 2012, 2013; Chira et al. 2014).

Located at a distance of 2.04 kpc (Hachisuka et al. 2006), the W3(OH) complex, consisting of two objects: W3(OH) itself and W3(H₂O), is one of the well-studied high-mass star-forming regions. W3(OH) is associated with an ultracompact (UC) H II region powered by an O7 star (Dreher & Welch 1981; Wilner, Welch & Forster 1995), while W3(H₂O) is rich in H₂O maser emission and organic molecules (Alcolea et al. 1993; Wyrowski et al. 1999;

*E-mail: slqin@bao.ac.cn

Hernández-Hernández et al. 2014; Qin et al. 2015), suggesting that it is at an earlier evolutionary stage. The observations suggest that W3(H₂O) has a mass of 10–20 M_⊙ and a luminosity of 10³–10⁴ L_⊙ (Wilner et al. 1995). High-angular resolution observations of the continuum and CH₃CN lines resolve W3(H₂O) into three sub-components: A, B, and C; with A and C likely forming a binary system (Wyrowski et al. 1999; Chen et al. 2006). Non-thermal radio jets and water maser outflows have been revealed with VLA and VLBA (Alcolea et al. 1993; Reid et al. 1995; Wilner, Reid & Menten 1999) observations along the east–west direction centred on W3(H₂O). Two CO molecular outflows (with PA=40° and 15°) and probably a rotating disc, have been studied in the W3(H₂O) with interferometers (Zapata et al. 2011). Single-pointing spectral line surveys reveal infall motions in the W3(OH) complex (e.g. Wu & Evans 2003; Wu et al. 2010), but the infalling centre and the gas accretion rate have not been well determined. The kinematics of W3(OH) are still under debate. OH masers and NH₃ absorption features suggest a collapsing outer envelope (Reid et al. 1980; Guilleloteau, Stier & Downes 1983; Garay, Reid & Moran 1985; Keto, Ho & Reid 1987), while expansion motions were proposed based on OH maser observations and multi-epoch VLA observations (Bloemhof, Reid & Moran 1992; Kawamura & Masson 1998).

In this paper, we present HCN and HCO⁺ line observations of the W3(OH) star-forming complex obtained with the Submillimeter Array (SMA)¹ and Caltech Submillimeter Observatory (CSO). The results show kinematical differences between the W3(H₂O) and W3(OH), in which infall motion seems to occur only towards the W3(H₂O) with evidence for jet procession, while gas expansion is observed towards W3(OH).

2 OBSERVATIONS

The SMA was used to observe the HCN (3–2) and HCO⁺ (3–2) transitions at 267 GHz. We summarize here the main aspects of the observations, while further details and the data reduction process can be found in Qin et al. (2015). The observations cover the HCN (3–2) and HCO⁺ (3–2) transitions at 267 GHz, with a spectral resolution of 0.406 MHz (corresponding to ~0.5 km s⁻¹). The weather conditions were good during the observations resulting in system temperatures of around 200 K. Flux calibration was performed using Uranus and we estimate an uncertainty of 20 per cent. The rms (1σ) noise level is 0.15 Jy beam⁻¹.

Single-dish observations of HCN (3–2) were obtained using the 10.4 m telescope at the CSO, on 2003, January 15. We covered an area of 110 arcsec × 110 arcsec, with 10 arcsec spacing. The beam size and main beam efficiency are 28 arcsec and 60 per cent, respectively. These observations were used to complement the missing short spacing information of the HCN (3–2) SMA observations. The CSO data were converted to Miriad format. The task MOSMEM was used to perform a joint deconvolution of the interferometric and single-dish data. The resulting combined data set has a spatial resolution of ~2.3 arcsec × 2.1 arcsec (PA=-60°) with robust weighting, and a sensitivity of 0.17 Jy beam⁻¹, with 1 Jy beam⁻¹ corresponding to a main beam brightness temperature of ~3.5 K.

¹ The SMA is a joint project between the Smithsonian Astrophysical Observatory and the Academia Sinica Institute of Astronomy and Astrophysics and is funded by the Smithsonian Institution and the Academia Sinica.

3 RESULTS

3.1 Gas distribution

3.1.1 HCN spectra obtained with the CSO

The W3(H₂O) hot core was first studied in the HCN (1–0) line at 89 GHz by Turner & Welch (1984). However, their observations lack a good spectral resolution (4.1 km s⁻¹), and cannot resolve detailed kinematics. The single pointing CSO observations of W3(OH) by Wu & Evans (2003) show that the HCN (3–2) line has a double peak, with the blue-shifted peak being stronger than the red-shifted one (hereafter ‘blue profile’), while the H¹³CN (3–2) line peaks at the absorption dip of the HCN (3–2), which was used by the authors to identify W3(OH) as a collapsing candidate object. However, their low-spatial resolution observations cannot determine the centre of collapse. Our CSO observations of the HCN (3–2) line, covering an area of 110 arcsec × 110 arcsec, are shown in Fig. 1. The ‘blue-profile’ is not only seen towards the central position but also towards a large area, suggesting that the W3(OH) complex is overall undergoing collapse, similar to what is observed in the G10.6–0.4 star-forming region (Liu et al. 2013).

3.1.2 Channel maps and velocity field

Fig. 2 shows the velocity channel map of the HCN (3–2) line at 265.886 GHz as observed with the SMA (green contours). The combined SMA and CSO data (SMA+CSO, red contours) are overlaid. The structure of the emission is the same in the SMA and SMA+CSO data sets in the velocity ranges from -69 to -53 km s⁻¹ and from -42 to -29 km s⁻¹. Around the systemic velocity of the cloud (i.e. from -52 to -43 km s⁻¹), the distribution of the gas consists of compact and diffuse components. As expected, the SMA data pick up the compact component well, while the diffuse gas is only detected with the CSO single-dish observations. A velocity gradient is seen in the channel maps, with a blue-shifted (from -69 to -56 km s⁻¹) component to the north-east of the W3(H₂O), and a red-shifted component (from -40 to -32 km s⁻¹) to the south-west. At around -47 to -46 km s⁻¹, we identify a flattened structure, without diffuse emission, elongated in the south-east–north-west direction. This velocity range is close to the self-absorption peak (see Section 3.2.2 and Fig. 3) for the HCN (3–2) line, suggesting that it traces a high-obscured part of the core, therefore likely locates at the centre of the dense core. This structure is perpendicular to the high velocity blue and red-shifted gas, which might indicate the presence of a disc (or toroid) and outflow system. In general, the gas is mainly associated with W3(H₂O), suggesting that HCN high velocity gas is most likely related to the presence of W3(H₂O) rather than W3(OH). In addition to the high velocity gas associated with W3(H₂O), emission from -44 to -40 km s⁻¹ reveals a north–south velocity gradient across W3(OH) which is consistent with the CH₃OH line as reported in Qin et al. (2015) and with the 6.7 GHz CH₃OH maser observations of Menten et al. (1992).

3.1.3 Spectra obtained with the SMA

In Fig. 3, we show the HCN spectrum obtained after combining the SMA and CSO data (SMA+CSO, black line), and the HCN, HCO⁺, HCN v₂=1 spectra as observed with the SMA (red, green, and blue lines) towards the W3(H₂O) and W3(OH) continuum peaks. Both HCN and HCO⁺ spectra towards the W3(H₂O) and W3(OH) show double peak line profiles while weak HCN v₂=1 line is only seen

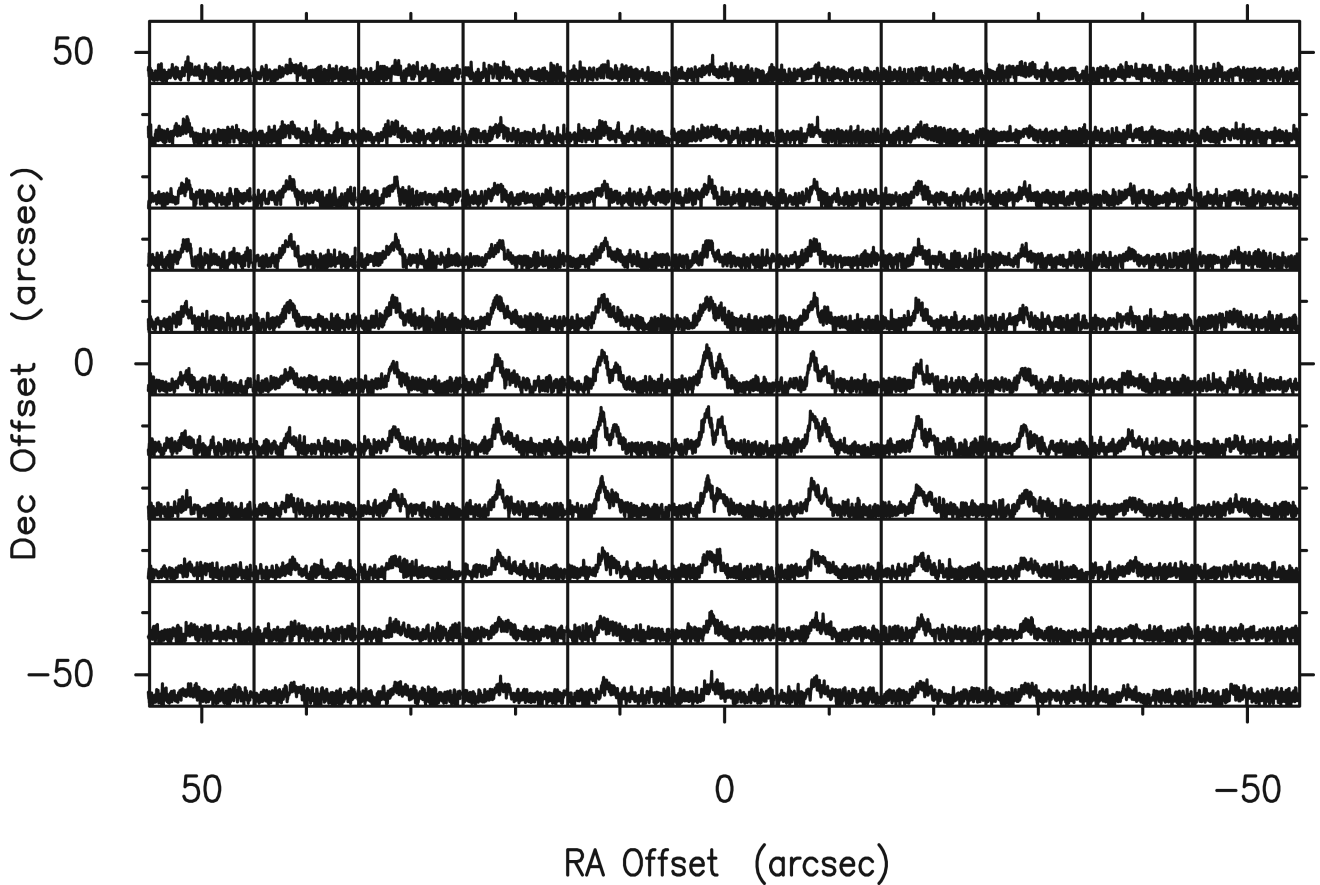


Figure 1. CSO HCN (3–2) spectral line observations. The mapped area covers an extension of 110 arcsec \times 110 arcsec, with 10 arcsec spacing. The beam size of the telescope at 267 GHz is \sim 28 arcsec.

towards the W3(H₂O). In principle, higher energy transitions can only be excited in the hot regions while lower energy transitions present in the cold surrounding regions, but also in the hot regions. Qin et al. (2015) argued that non-detection of HCN $v_2=1$ towards the W3(OH) is due to the fact that the gas seen in the W3(OH) comes from the outer region of the UC H II region and inner portion of this hot core has been dissociated by the stars, and lower HCN abundance and gas temperature of envelope make the HCN $v_2=1$ too weak and expected intensity is lower than the SMA detection limit. The broad line is seen in HCN but not in HCO⁺ towards the W3(H₂O) (see top panel of Fig. 3), suggesting that HCN is better tracing the molecular outflow of this region. Both HCN and HCO⁺ show an absorption dip at around -47.8 km s⁻¹, with the blue-shifted peak being stronger (‘blue profile’ asymmetry). On the other side, the HCN $v_2=1$ line peaks at around ~ -49 km s⁻¹, i.e. near the position of the absorption dip. The bottom panel of Fig. 3 shows the spectra towards the W3(OH) continuum peak position. Differently to the case of W3(H₂O), the spectra are prominently red-shifted, i.e. with the red-shifted peak being stronger than the blue-shifted one. This kind of profiles are indicative of gas expansion (e.g. Aguti et al. 2007).

The combined SMA+CSO spectrum at the W3(H₂O) continuum peak (top panel of Fig. 3) is only slightly stronger than the SMA-only spectrum, indicating that even with only the SMA we are recovering most of the HCN emission, as expected for a tracer of compact and dense gas. The blue side of the SMA spectrum at the W3(OH) continuum peak is much weaker than that of the

SMA+CSO data. Previous observations of single dish and interferometers (Mauersberger, Wilson & Henkel 1988; Wilson, Johnston & Mauersberger 1991; Wilson, Gaume & Johnston 1993; Wink et al. 1994) suggested that the W3(OH) complex consists of extended envelope with lower gas density of $\sim 10^5$ cm⁻³ and the compact core W3(H₂O) with gas density of $\sim 10^7$ cm⁻³. The critical density of HCN (3–2) is at one order of $\sim 10^7$ cm⁻³ (at ~ 50 K), so one should see similar spectral profile at the W3(H₂O) position with the SMA and SMA+CSO. This is also verified from the channel maps (see Fig. 2), in which compact clumps observed by the SMA and SMA+CSO have almost same morphology and extended emission located outside of the compact clumps can only be seen by the SMA+CSO data. As for the W3(OH), the weakness of blue side of the HCN spectrum observed with the SMA should be caused by the filtering effect of the interferometer in which lower density gas in front of H II region should show blue-shifted emission if the cloud is in expansion, but can be recovered by single dish observations.

The different line profiles may reflect different kinematics between the W3(H₂O) and W3(OH). In Sections 3.2.2 and 3.3, we discuss the nature of these profiles.

3.2 Kinematics in W3(H₂O)

Observations showed that molecular line emissions mainly arise from the W3(H₂O) core with higher gas density while absorption lines are observed in the W3(OH) which have lower density

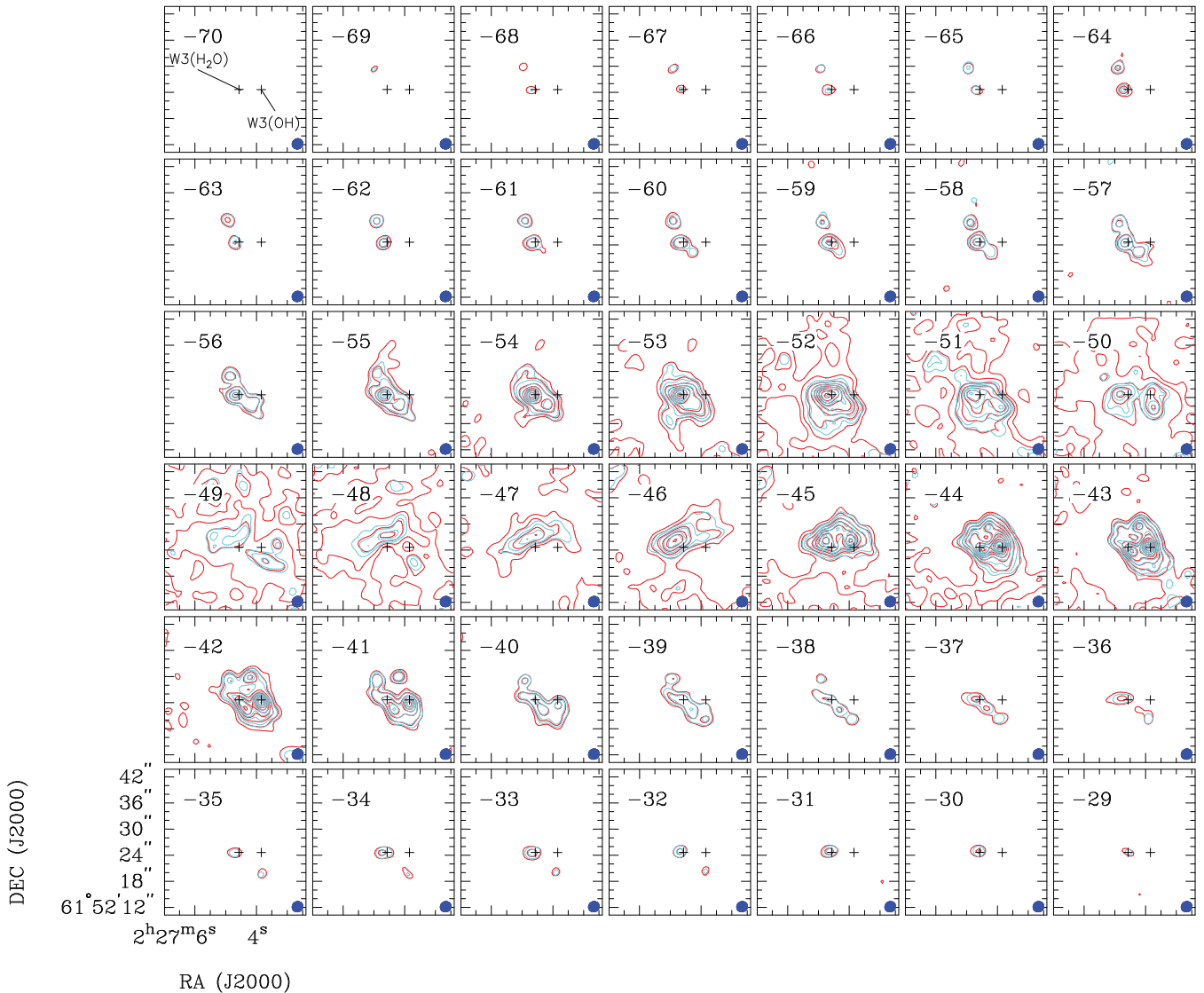


Figure 2. Channel maps of the HCN (3–2) transition from the combined SMA and CSO data sets (red contours) and from the SMA data set alone (turquoise contours). The contours are 5, 10, 20, 30, 40, 50, 60, 70, 80, 90 per cent of the peak intensities, $12.7 \text{ Jy beam}^{-1}$ for SMA+CSO and $12.2 \text{ Jy beam}^{-1}$ for SMA. The rms (σ) noise levels for SMA+CSO and SMA data are 0.17 and $0.15 \text{ Jy beam}^{-1}$, respectively. In each panel, the synthesized beam is shown in bottom-right corner, and the cross symbols indicates the peak positions of the W3(H₂O) and W3(OH) continuum sources (Qin et al. 2015).

(Mauersberger et al. 1988; Wilson et al. 1991, 1993; Wink et al. 1994). The two sources are spatially separated and have different systemic velocities (Wilson et al. 1991; Qin et al. 2015), implying different physics and kinematics. At a large scale, the two sources share same envelope and the background sources will affect the observed optically thick line shapes in both line profile and intensity if the background source has different kinematics. We think these will not obviously affect the observed line shape and intensity of the W3(H₂O) since higher density gas dominates kinematics of the compact core as seen from Figs 2 and 3. 90 per cent of the molecular matter associated with the W3(OH) is located behind or to the side of the W3(OH) H II region (Wilson et al. 1991). Thus one should see ‘red asymmetry’ line profile of HCN and HCO⁺ with comparable red peak line intensity observed by the SMA and SMA+CSO. An alternative explanation of the line profile towards the W3(OH) is that W3(OH) may be located behind W3(H₂O) and the blue-shifted HCN emission towards this source is absorbed by the dense envelope of the W3(H₂O), producing the observed red asymmetry. If so,

one should see similar velocity pattern as in the W3(H₂O). But the blue-shifted peak velocities between the two cores are different (see Fig. 3), thus the observed ‘red asymmetry’ line profile supports gas expansion in the W3(OH) region.

3.2.1 Molecular outflows

Previous observations of the CO (2–1) line show two large-scale bipolar outflows driven by the W3(H₂O)-A and C sources (Zapata et al. 2011). Compared to the CO transition, HCN (3–2) has a higher critical density and should trace compact outflows close to the exciting sources. Fig. 4 presents the HCN velocity-integrated intensity map of the SMA+CSO HCN line. Both the blue and red-shifted gas have three emission clumps. The clumps located close to W3(H₂O) are likely associated with W3(H₂O)-A, while the other clumps are located to the north-east and south-west of the W3(H₂O)-C source, suggesting that they are tracing an outflow powered by source C. The outflow has a position angle of 54° . Assuming that the

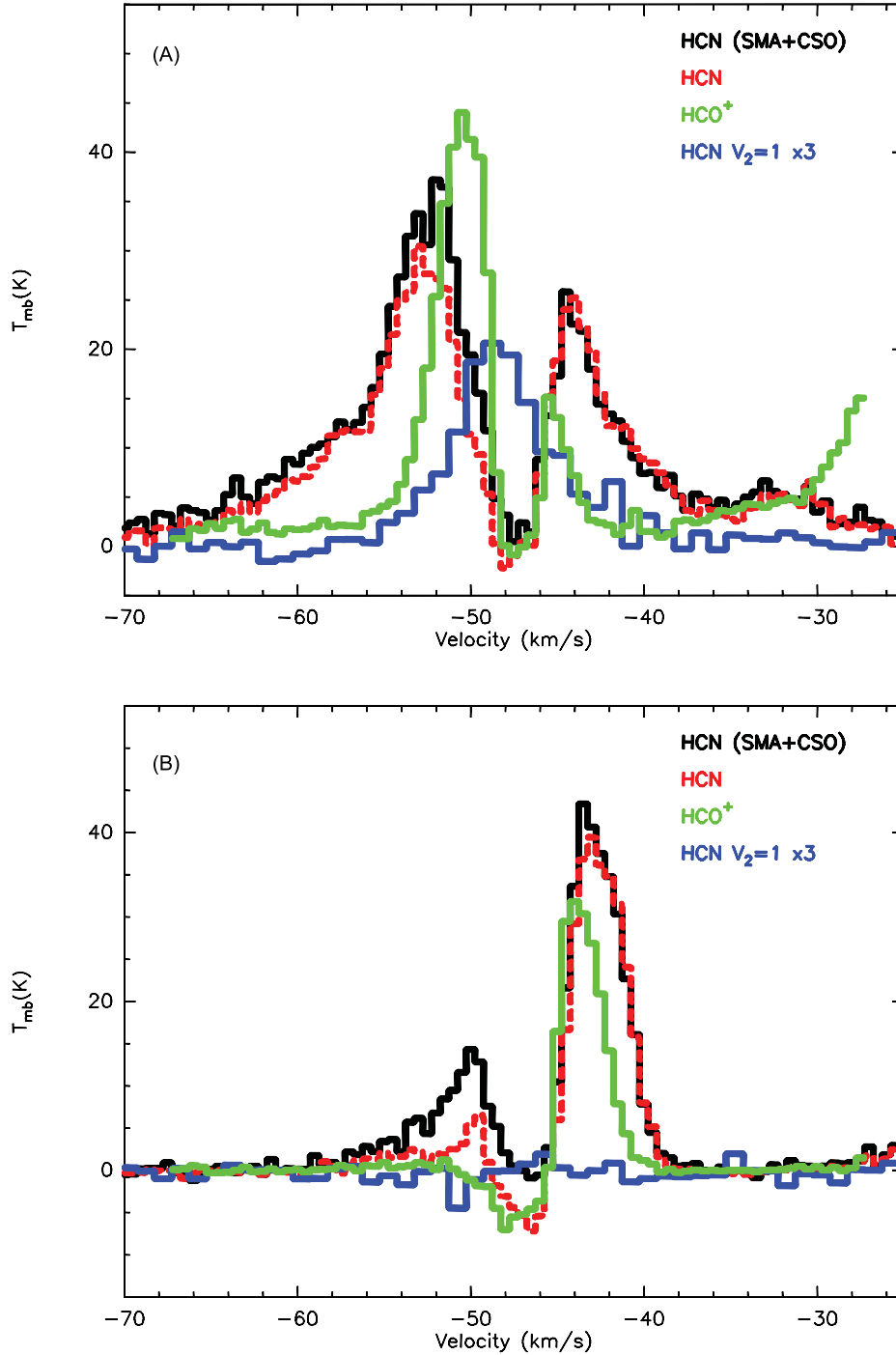


Figure 3. Top panel: spectra extracted towards the W3(H₂O) continuum peak (see Qin et al. 2015) for HCN (SMA+CSO, black line), HCN (only SMA, red dashed line), HCO⁺ (green line), and HCN $v_2=1$ (blue line). Bottom panel: same as for the top panel towards the W3(OH) continuum peak.

HCN line wing emission is optically thin, an excitation temperature of 50 K (as in Zapata et al. 2011), and an HCN abundance of 9.6×10^{-9} (Qin et al. 2015), under local thermodynamic equilibrium, we infer an outflow mass of $2.6 \pm 0.3 M_{\odot}$ with some uncertainties due to the assumptions of optically thin emission, excitation temperature and fractional abundance of HCN. The estimated dynamic time of the outflow is $(5.6 \pm 0.2) \times 10^3$ yr, and the mass-loss rate is $\sim (4.6 \pm 0.5) \times 10^{-4} M_{\odot} \text{ yr}^{-1}$.

3.2.2 Infall motion

The HCN and HCO⁺ SMA spectra towards the W3(H₂O) continuum peak position show an absorption dip at around the systemic velocity (-47.8 km s^{-1} , see Fig. 3-top). This absorption dip is also visible in the single-dish data (see fig. 1 of Wu & Evans 2003), indicating that it is not caused by interferometric spatial filtering. Another possible explanation is the presence of two different

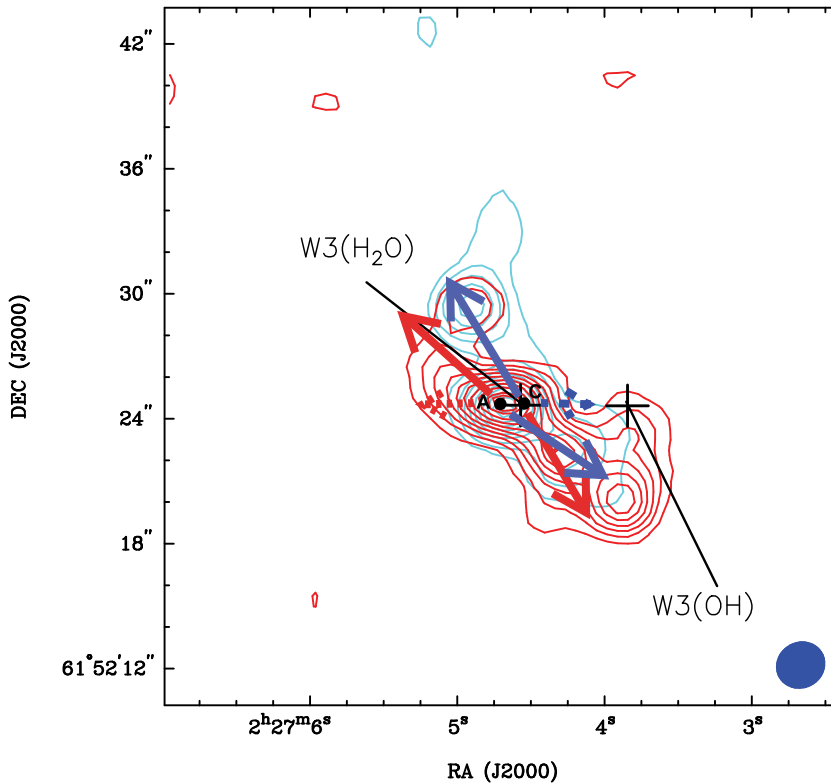


Figure 4. HCN outflow image from the CSO+SMA data. The blue-shifted emission (blue contours) show the emission integrated from -69 to -56 km s^{-1} , while the red-shifted (red contours) show the emission from -40 to -32 km s^{-1} . The contours levels of both the blue (peak value of 20.6 $\text{Jy beam}^{-1} \text{ km s}^{-1}$) and red lobes (14.8 $\text{Jy beam}^{-1} \text{ km s}^{-1}$) range from 10 to 100 per cent of the peak emission. The crosses indicate the peak positions of the W3(H₂O) and W3(OH) continuum (Qin et al. 2015). The filled circles denote the W3(H₂O)-A and C source positions. The synthesized beam is shown in bottom-right corner. The blue and red arrows denote the orientation of CO molecular outflows (Zapata et al. 2011). The dashed arrows indicate the orientation of non-thermal jets and water maser outflows (Alcolea et al. 1993; Reid et al. 1995)

velocity components, but this is ruled out when examining the higher energy transition of HCN $v_2=1$, which is expected to be optically thin and shows a single peak at the position of the absorption dip (see Fig. 3-top). Therefore, the profile seen in the HCN and HCO⁺ lines is likely due to these lines being optically thick. Moreover, the blue-shifted peak is stronger than the red-shifted one, showing ‘blue profile’ asymmetry. The classical ‘blue asymmetry’ says that the optically thin will peak in the middle of absorption dip of the optically thick line if the emission is from a single source. But in the W3(H₂O) case, higher angular observations of continuum and lines have resolved W3(H₂O) into A and C subcomponents with different systemic velocities, in which sources A and C have systemic velocities of -51.4 and -48.6 km s^{-1} (Chen et al. 2006), and -50.5 and -46.5 km s^{-1} (Zapata et al. 2011), respectively. The HCN $v_2=1$ line presents east–west velocity gradient (Qin et al. 2015) and the emission may contribute from both sources A and C. Therefore, the peak velocity of HCN $v_2=1$ does not peak at the HCN absorption dip. Our ‘two-layer model’ gave a medium value of -47.8 km s^{-1} (see next paragraph) between -48.6 and -46.5 km s^{-1} of C component, indicating that gas is falling on to the W3(H₂O)-C. Following Mardones et al. (1997), we use the asymmetry parameter δv – the velocity difference between the peaks of the optically thick line (v_{thick}) and the optically thin (v_{thin}) lines – to quantify the blue asymmetry of the HCN and HCO⁺ lines in W3(H₂O). The parameter is defined as $\delta v = (v_{\text{thick}} - v_{\text{thin}}) / \Delta v_{\text{thin}}$, with Δv_{thin} being the line width of the optically thin HCN $v_2=1$. An statistically significant excess of blue

asymmetric line profiles with $\delta v < -0.25$ indicate that the molecular gas is infalling on to the cores (e.g. Mardones et al. 1997; Wu & Evans 2003; Fuller, Williams & Sridharan 2005; Wu et al. 2007). Gaussian fitting is made to the HCN (3–2), HCO⁺ (3–2), and HCN $v_2=1$ lines. The resulting δv for HCN (3–2) and HCO⁺ (3–2) are -0.65 and -0.38 , respectively. These values indicate gas infalling towards the W3(H₂O) continuum core.

Although the asymmetry parameters derived from both HCN (3–2) and HCO⁺ (3–2) lines suggest gas infalling motion, the HCN spectrum in the W3(H₂O) may be confused by the outflows as seen from Fig. 2 and 3. In the case of HCO⁺ (1–0), the interferometer see 40 per cent of the single dish flux (Wink et al. 1994). HCO⁺ (3–2) has larger critical density compared to HCO⁺ (1–0) and should recover more flux of the single dish observations. In order to quantify the infall rate, we modelled the ‘blue profile’ HCO⁺ spectrum using a two-layer model (see appendix, and Myers et al. 1996; Di Francesco et al. 2001). The model fits the observed spectrum by setting the background temperature of the continuum source, the excitation temperature, the beam filling factor, the systemic velocity, the infall velocity, the velocity dispersion, and the peak optical depth. The best fit to the HCO⁺ spectrum (see Fig. 5) results in an infall velocity (V_{in}) of 2.7 ± 0.3 km s^{-1} and a velocity dispersion of 0.8 ± 0.1 km s^{-1} . Similar to the work done by Pineda et al. (2012), we assume that the gas is in a spherically symmetric free fall on to the W3(H₂O) core. Therefore, we can estimate the mass infall rate ($\dot{M} = 3V_{\text{in}}^3/2G$) to be $(2.3 \pm 0.7) \times 10^{-3} M_{\odot} \text{ yr}^{-1}$.

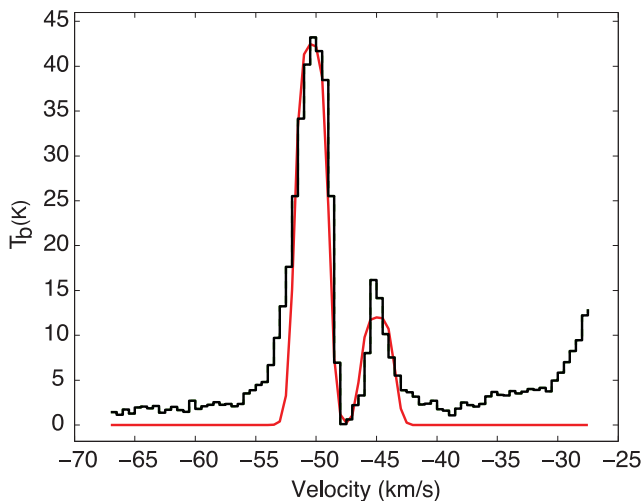


Figure 5. Observed HCO⁺ (black line) and two-layer model (red) spectra towards the W3(H₂O) continuum peak position (see Qin et al. 2015).

3.3 Expansion in W3(OH)

Fig. 6 (left-hand panel) shows the HCN spectrum (CSO+SMA) at the W3(OH) continuum peak position. It shows an absorption dip at around the systemic velocity (-46.4 km s^{-1}) with the red-shifted peak being stronger than the blue-shifted one (‘red profile’), suggestive of expansion. In the right-hand panel, we show the HCO⁺ spectrum, which reveals a P-cygni profile. The two-layer model (Myers et al. 1996) was used to fit the observed ‘red profile’ and determine the expansion velocity. Note that we set same filling factor and background temperature for the HCN and HCO⁺ lines in the model. The mean expansion velocities are estimated to be $3.8 \pm 0.4 \text{ km s}^{-1}$ and $1.6 \pm 0.2 \text{ km s}^{-1}$ from the HCN (CSO+SMA) and HCO⁺ lines (SMA), respectively. The critical density of HCN (3–2) is one order of magnitude higher than that of HCO⁺ and then one expects HCN to be more opaque in denser regions (Wu & Evans 2003; Reiter et al. 2011). HCN and HCO⁺ are likely tracing different layers of the cloud, which lead to different expansion velocities. More quantitative analyses by use of radiative transfer model such as RATRAN (Hogerheijde & van der Tak 2000) are needed. As done by

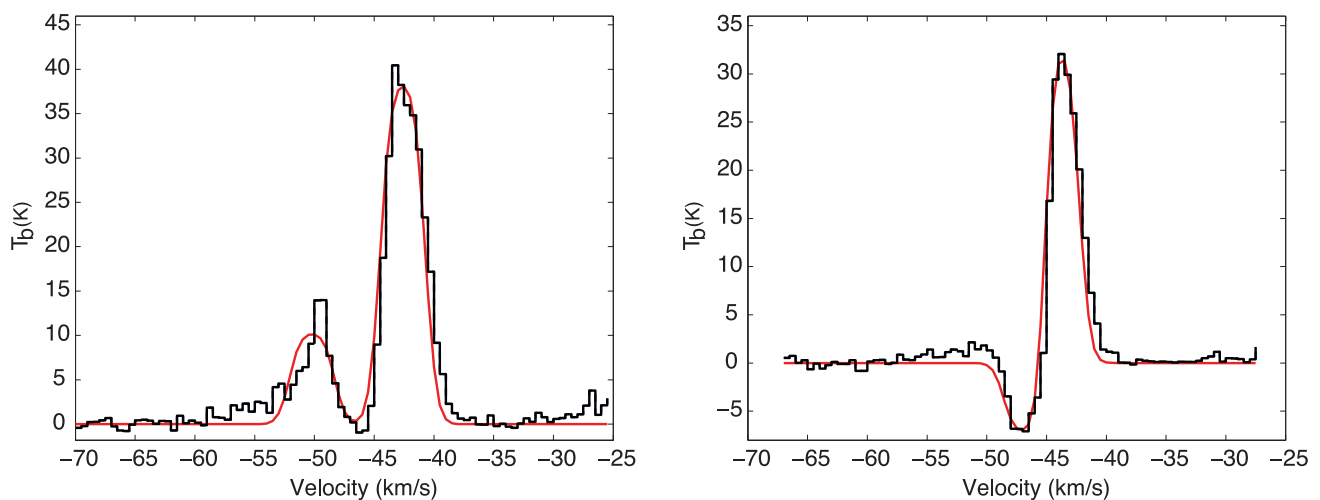


Figure 6. HCN (left-hand panel, from CSO+SMA data sets) and HCO⁺ (right-hand panel, from SMA data set) spectra towards the W3(OH) continuum peak position (see Qin et al. 2015). Left-hand panel: observed (black line) and two-layer model (red) HCN spectra. Right-hand panel: observed (black) and two-layer model (red) HCO⁺ spectra.

Rolfs et al. (2010), modelling multiple transitions of HCN or HCO⁺ spanning a wide energy levels with different opacities can constrain velocity field, abundance and density profiles, and kinematics well. Currently the density and temperature profiles are only obtained towards the W3(H₂O) core (Chen et al. 2006). Observations of multilevel transitions of the HCN or HCO⁺ are needed to obtain the physical and kinematical structures towards the W3(OH) complex in the future.

IRAC data were retrieved from the data base of Galactic Legacy Infrared Midplane Extraordinaire (Churchwell et al. 2009). In Fig. 7, we present the flux ratio map of the *Spitzer*/Infrared Array Camera (IRAC) 4.5 to 3.6 μm emission (in colour scale) overlaid with the SMA 1.1 mm continuum emission (in contours) towards the W3(OH) complex. The observations and analyses suggested that the morphologies observed at 3.6 and 4.5 μm are similar to each other and to H₂ 1–0 S(1) line, and thus the emissions of the 4.5 and 3.6 μm bands include bright H₂ lines (e.g. Cyganowski et al. 2009; Takami et al. 2010) compared to the other bands of the *Spitzer*/IRAC instrument. It is thought that a 4.5 to 3.6 μm flux ratio larger than 1.5 traces shocked gas (e.g. Takami et al. 2010). As shown in the Fig. 7, both the 4.5 and 3.6 μm images are saturated within the 1.1 mm continuum emission (the region encompassed by the pink circle), and a reliable ratio image cannot be obtained. However, the ratio can be determined in the non-saturated pixels. Values of the ratio >1.5 are found in an area of diameter ~ 50 arcsec. The ratio map shows a gradient distribution decreasing towards the outer regions, with the largest values found around the W3(OH) continuum source. This result might indicate large-scale shocks in the region. Interestingly, pixels with ratios larger than three are found in three ring-like structures surrounding the W3(OH) continuum peak, mainly distributed to the south. This can be interpreted as the ambient gas not being uniform, if the shocked material is due to the expansion of the H II region.

4 DISCUSSION

4.1 Outflows and infall

At least two CO molecular outflows are identified in the W3(OH) complex, likely driven by the sources W3(H₂O)-A and C (Zapata

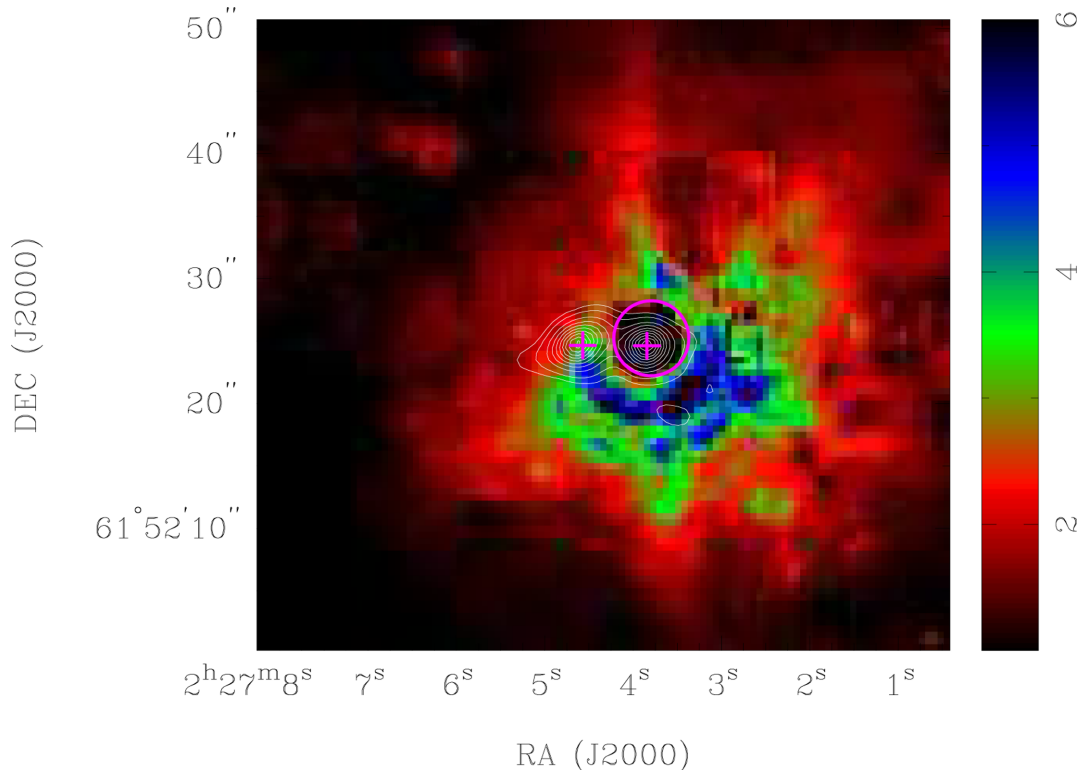


Figure 7. *Spitzer*/IRAC 4.5 μm -to-3.6 μm ratio image (colour scale) overlaid with the SMA 1.1 mm continuum map (contours). The crosses indicate the peak positions of the W3(H₂O) and W3(OH) continuum sources. Note that the *Spitzer*/IRAC 4.5 μm and 3.6 μm images are saturated at the position of W3(OH) continuum as encompassed by the pink circle symbol.

et al. 2011). In comparison, the outflows that we have detected in the HCN (3–2) transition show a smaller spatial extension and outflow mass, which could be explained by the fact that the CO traces large-scale and extended outflowing material. The directions of the outflows determined for both HCN and CO outflows are consistent (see arrows in Fig. 4), associated with W3(H₂O)-C, and show multiple knots in the red and blue-shifted lobes. So far, only a few massive outflows associated with high-mass star-forming regions have been observed to show a discrete knotty structure (e.g. Qiu & Zhang 2009; Sánchez-Monge et al. 2014). One possible interpretation is that the HCN outflows in our observations are made of swept-up ambient gas originated from an episodic and precessing mass-loss process (Arce & Goodman 2001). Non-thermal radio jets and water maser outflows along the east–west direction (PA = 90°) revealed by the VLA and VLBI observations (e.g. Wilner et al. 1999), two CO molecular outflows (with PA \sim 40° and \sim 15°; Zapata et al. 2011) and our HCN outflows (PA \sim 54°) suggest that different tracers trace different kinematics of the outflows, providing another evidence for jet precession in the W3(H₂O). A binary system (and disc candidates) has been reported in the W3(H₂O) (e.g. Wyrowski et al. 1999; Chen et al. 2006; Zapata et al. 2011). It has been proposed that episodic and precessing outflows might be related to the presence of a binary system (e.g. Arce & Goodman 2001). Therefore, episodic and precessing outflows in the W3(H₂O) might be related to the presence of a binary system. The lack of an H II region in W3(H₂O), the presence of strong dust emission and the derived short outflow time-scale of $(5.6 \pm 0.2) \times 10^3$ yr, compared with other high-mass molecular outflows (e.g. Beuther et al. 2002; Wu et al. 2004; Zhang et al. 2005; Sánchez-Monge et al. 2013b), suggest that the W3(H₂O) could be in an early evolutionary stage of the high-mass star formation process.

Spectral infall signatures are seen in W3(H₂O), and an unusually large spherical mass infall rate of $(2.3 \pm 0.7) \times 10^{-3} M_{\odot} \text{ yr}^{-1}$ is derived. Recent observations have revealed high-mass accretion rates (10^{-3} – $10^{-2} M_{\odot} \text{ yr}^{-1}$) in other high-mass star-forming regions (e.g. Sandell, Goss & Wright 2005; Garay et al. 2007; Zapata et al. 2008; Wu et al. 2009; Rolffs et al. 2010; Liu et al. 2011a, 2013). This work predicts comparable accretion rates, suggesting high-mass stars are forming in W3(H₂O). Adopting an H₂ number density of 10^8 cm^{-3} (Chen et al. 2006), and assuming that the collapse is uniform, pressure-free, and non-rotating, the free-fall time-scale ($t_{\text{ff}} = \sqrt{3\pi/(32G\rho)} = 5 \times 10^7 / \sqrt{n(\text{H}_2)}$) is estimated to be 5×10^3 yr, which is consistent with the outflow time-scale. The assumptions are reasonable since the derived density profile of W3(H₂O) support free-fall collapse (Chen et al. 2006). The infall velocity derived from a two-layer collapse model fit to the HCO⁺ (3–2) line is $2.7 \pm 0.3 \text{ km s}^{-1}$. Assuming that the velocity dispersion ($0.8 \pm 0.1 \text{ km s}^{-1}$) is caused by thermal motions, the large infall velocity suggests that collapse is proceeding in a supersonic way. Chen et al. (2006) derived the W3(H₂O)-A and C systemic velocities of -51.4 and -48.6 km s^{-1} , respectively, while Zapata et al. (2011) derive systemic velocities of -50.5 and -46.5 km s^{-1} for the A and C sources. Our two-layer model fitting to the HCO⁺ line results in a systemic velocity of -47.8 km s^{-1} , which seems to indicate that the gas is infalling on to the W3(H₂O)-C.

4.2 Expansion

Based on the relative proper motions of the OH maser spots observed at different epochs towards W3(OH), Bloemhof et al. (1992) proposed gas expansion from the UC H II region to explain the observed pattern of motions. Furthermore, a direct measurement of

expansion of the W3(OH) was made through the different difference maps obtained by the VLA at three epochs (Kawamura & Masson 1998). They suggest that the shell-like H II region is slowly expanding with a typical speed of $3\text{--}5 \text{ km s}^{-1}$ and derive a dynamical age of $\sim 2300 \text{ yr}$.

The HCN red profile and HCO^+ P-cygni profile towards the W3(OH) continuum peak position suggest that the gas in the envelope is expanding (see Fig. 6). The two-layer model results in mean expansion velocities of 3.8 ± 0.4 and $1.6 \pm 0.2 \text{ km s}^{-1}$, respectively. Considering the different critical densities of the two transitions, this suggests that the expansion of the envelope is decelerating. Flux ratio map of *Spitzer*/IRAC 4.5 and $3.6 \mu\text{m}$ images shows a radial distribution from inside to outside, with the largest ratios found around the W3(OH) continuum source, likely pinpointing W3(OH) as the expansion centre. Ratios larger than 1.5 indicate shocked gas, likely produced by the interaction of the expanding H II region and the molecular cloud. At the distance of W3(OH) (2.2 kpc; Hachisuka et al. 2006), the shock radius of 25 arcsec (see Fig. 7) and the expanding velocity of $3.8 \pm 0.4 \text{ km s}^{-1}$ (derived from HCN line) result in an expanding time-scale of about $(6.4 \pm 0.7) \times 10^4 \text{ yr}$. This value is larger than the time-scale of 2300 yr derived by Kawamura & Masson (1998), but lower than the typical age of 10^5 yr for UCH II regions. We do think that the expansion time-scale of W3(OH) as derived in this work is reasonable, since the time-scale of infall and outflow motions in the W3(H₂O) is approximately $5 \times 10^3 \text{ yr}$, and W3(H₂O) is likely at an earlier evolutionary stage compared to W3(OH).

4.3 Dynamical state of the W3(OH) complex

The W3(OH) complex is an nearby star formation region harbouring two sites of high-mass star formation, W3(H₂O) and W3(OH), with different properties. W3(H₂O) is rich in water masers and organic molecules, and at earlier evolutionary stage compared to W3(OH),

which is associated with an UCH II region and is rich in OH masers. Previous observations of OH masers and NH₃ absorption features suggest a collapsing outer envelope outside the UCH II region. Our CSO grid spectra of the HCN (3–2) line (see Fig. 1) show a ‘blue profile’ in a large area suggesting that collapse is not happening only around the UCH II region but it is a global collapse in the W3(OH) complex.

At small scales, the two sources have different kinematics, based on both previous studies and the observations presented in this work. A small-scale non-thermal radio jet and water maser outflows along the east–west direction together with large scale CO outflows and a rotating disc candidate have been reported towards W3(H₂O) in previous works. Complementary to this, our HCN and HCO^+ line results show infall and outflow motions, and a flattened structure perpendicular to the direction of the outflows. At the same time, relative proper motions of OH maser spots and multi-epoch radio continuum maps suggest the presence of expansion motions originated from the W3(OH) UCH II region. Our molecular line observations, combined with *Spitzer*/IRAC images confirm the expansion interpretation with W3(OH) being located at the centre. From the expansion velocity derived with the two-layer model fit and the size of the shocked gas as revealed by the IRAC images, we determine an expansion time-scale of $(6.4 \pm 0.7) \times 10^4 \text{ yr}$.

Based on the above statements, we present a sketch of the dynamical state of the W3(OH) complex in Fig. 8. We describe the picture in the following. The W3(OH) complex harbours W3(H₂O) and W3(OH), with W3(H₂O) being in an earlier evolutionary stage of massive star formation compared to W3(OH), who has already developed an H II region. Far from the forming stars, the outer envelope of the W3(OH) complex is collapsing inwards. Inside the complex, W3(H₂O) is still undergoing collapse and is associated with collimated outflowing material. On the other side the H II region of W3(OH) is expanding and driving a shock front into the ambient material, which leads to the observed neutral gas expansion and shock.

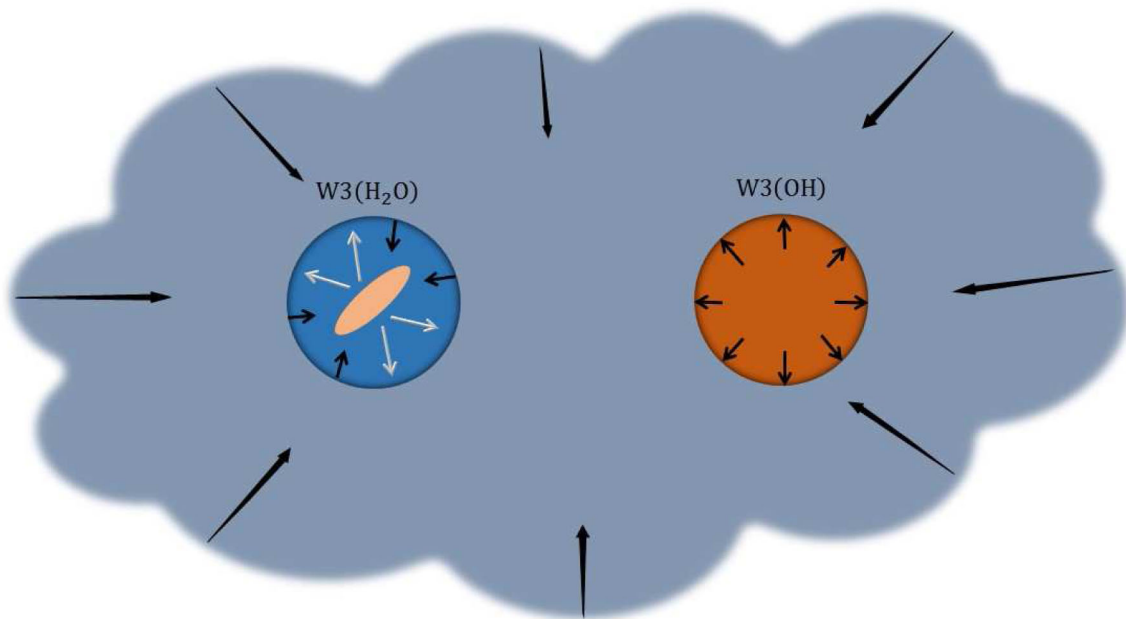


Figure 8. Sketch of dynamical state of the W3(OH) star-forming complex. The molecular cloud harbouring the W3(OH) and W3(H₂O) regions is globally collapsing. Gas expansion is seen towards W3(OH) due to the expansion of the H II region. At the position of W3(H₂O) there is infall (black arrows), outflows (white arrows), and a possible rotating disc (yellow ellipse).

5 SUMMARY

We have carried out SMA and CSO observations of different molecular tracers (HCN and HCO⁺ lines) towards the W3(OH) star-forming complex. The results are summarized in the following.

(i) The CSO grid spectral observations of HCN show a blue asymmetric profile over a large area covering the whole star-forming complex, which suggests that the outer envelope of the W3(OH) complex is undergoing global collapse.

(ii) The SMA (and SMA+CSO) observations reveal blue asymmetric line profiles for both HCN and HCO⁺ spectral lines towards the W3(H₂O) dust continuum core. A two-layer collapse model is used to fit the HCO⁺ line shape. The derived mass accretion rate is $(2.3 \pm 0.7) \times 10^{-3} M_{\odot} \text{ yr}^{-1}$. The free-fall time-scale is estimated to be 5×10^3 yr.

(iii) Bipolar outflows, identified in the HCN images, are likely driven by the source C in W3(H₂O). The molecular outflows show a knotty structure, which might be caused by an episodic and precessing process, likely related to the presence of a binary system in W3(H₂O). A mass-loss rate of $(4.6 \pm 0.7) \times 10^{-4} M_{\odot} \text{ yr}^{-1}$ is derived, larger than the typical values found in low-mass molecular outflows. The dynamic time-scale of the outflows is around $(5.6 \pm 0.2) \times 10^3$ yr, consistent with the free-fall time-scale. The large accretion and mass-loss rates, confirm the formation of high-mass stars in the W3(H₂O) region.

(iv) The red asymmetric profile of the HCN line together with the HCO⁺ P-cygni profile at the W3(OH) continuum peak, indicate that the envelope around this source is expanding. A two-layer model fit to the spectra results in expansion time-scales of $(6.4 \pm 0.7) \times 10^4$ yr. The *Spitzer*/IRAC 4.5 μm -to-3.6 μm flux ratio image is also consistent with the envelope around W3(OH) being in expansion, and shows a gradient distribution from inside to outside with largest values (i.e. more evidence of shock, likely related to a faster expansion) around the W3(OH) continuum source. We conclude that the W3(OH) H II region is expanding and interacting with the ambient gas, and the shocked neutral gas is decelerating expanding.

In summary, the W3(OH) complex is undergoing global collapse. Inside the complex, the two objects W3(H₂O) and W3(OH) are at different evolutionary stage of massive star formation. Infall and outflow motions are observed at an earlier stage in the W3(H₂O), while the W3(OH) H II region is expanding, which leads to observed neutral gas expansion and shock.

ACKNOWLEDGEMENTS

We thank the anonymous referee, and editor Morgan Hollis for their constructive comments on the paper. This work has been supported by the National Natural Science Foundation of China under grant Nos. 11373026, 11373009, 11433004, 11433008, U1331116, and the National Basic Research Program of China (973 Program) under grant No. 2012CB821800, by Top Talents Program of Yunnan Province (2015HA030) and Midwest universities comprehensive strength promotion project (XT412001, Yunnan university), by the Deutsche Forschungsgemeinschaft, DFG through project number SFB956.

REFERENCES

Aguti E. D., Lada C. J., Bergin E. A., Alves J. F., Birkinshaw M., 2007, *ApJ*, 665, 457

- Alcolea J., Menten K. M., Moran J. M., Reid M. J., 1993, in Clegg A. W., Nedoluha G. E., eds, *Lecture Notes in Physics*, Vol. 412, *Astrophysical Masers*. Springer-Verlag, Berlin, p. 225
- Arce H. G., Goodman A. A., 2001, *ApJ*, 554, 132
- Beuther H., Schilke P., Sridharan T. K., Menten K. M., Walmsley C. M., Wyrowski F., 2002, *A&A*, 383, 892
- Bloemhof E. E., Reid M. J., Moran J. M., 1992, *ApJ*, 397, 500
- Chen H.-R., Welch W. J., Wilner D. J., Sutton E. C., 2006, *ApJ*, 639, 975
- Chira R., Smith R. J., Klessen R. S., Stutz A. M., Shetty R., 2014, *MNRAS*, 444, 874
- Churchwell E. et al., 2009, *PASP*, 121, 213
- Cyganowski C. J., Brogan C. L., Hunter T. R., Churchwell E., 2009, *ApJ*, 702, 1615
- Di Francesco J., Myers P. C., Wilner D. J., Ohashi N., Mardones D., 2001, *ApJ*, 562, 770
- Dreher J. W., Welch W. J., 1981, *ApJ*, 245, 857
- Fuller G. A., Williams S. J., Sridharan T. K., 2005, *A&A*, 442, 949
- Garay G., Reid M. J., Moran J. M., 1985, *ApJ*, 289, 681
- Garay G. et al., 2007, *A&A*, 463, 217
- Guilloteau S., Stier M. T., Downes D., 1983, *A&A*, 126, 10
- Hachisuka K. et al., 2006, *ApJ*, 645, 337
- Hernández-Hernández V., Zapata L., Kurtz S., Garay G., 2014, *ApJ*, 786, 38
- Hogerheijde M. R., van der Tak F. F. S., 2000, *A&A*, 362, 697
- Jiang Z. B., Tamura M., Fukagawa M., Hough J., Lucas P., Suto H., Ishii M., Yang J., 2005, *Nature*, 437, 112
- Kawamura J. H., Masson C. R., 1998, *ApJ*, 509, 270
- Keto E., Ho P. T. P., Reid M. J., 1987, *ApJ*, 323, L117
- Liu T., Wu Y. F., Zhang Q., Ren Z., Guan X., Zhu M., 2011a, *ApJ*, 728, 91
- Liu T., Wu Y. F., Liu S.-Y., Qin S.-L., Su Y.-N., Chen H.-R., Ren Z., 2011b, *ApJ*, 730, 102
- Liu T., Wu Y. F., Wu J. W., Qin S.-L., Zhang H., 2013, *MNRAS*, 436, 1335
- Liu T. et al., 2015, *ApJ*, 810, 147
- Mardones D., Myers P. C., Tafalla M., Wilner D. J., 1997, *ApJ*, 489, 719
- Mauersberger R., Wilson T. L., Henkel C., 1988, *A&A*, 201, 123
- Menten K. M., Reid M. J., Pratap P., Moran J. M., Wilson T. L., 1992, *ApJ*, 401, L39
- Myers P. C., Mardones D., Tafalla M., Williams J. P., Wilner D. J., 1996, *ApJ*, 465, L133
- Patel N. A. et al., 2005, *Nature*, 437, 109
- Pineda J. E. et al., 2012, *A&A*, 544, L7
- Qin S.-L., Schilke P., Wu J. W., Wu Y., Liu T., Liu Y., Sánchez-Monge Á., 2015, *ApJ*, 803, 309
- Qiu K., Zhang Q., 2009, *ApJ*, 702, L66
- Reid M. J., Haschick A. D., Burke B. F., Moran J. M., Johnston K. J., Swenson G. W., Jr, 1980, *ApJ*, 239, 89
- Reid M. J., Argon A. L., Masson C. R., Menten K. M., Moran J. M., 1995, *ApJ*, 443, 238
- Reiter M., Shirley Y. L., Wu J. W., Brogan C., Wootten A., Tatsumatsu K., 2011, *ApJ*, 740, 40
- Rolfs R. et al., 2010, *A&A*, 521, L46
- Sánchez-Monge Á. et al., 2013a, *A&A*, 552, L10
- Sánchez-Monge Á., López-Sepulcre A., Cesaroni R., Walmsley C. M., Codella C., Beltrán M. T., Pestalozzi M., Molinari S., 2013b, *A&A*, 557, 94
- Sánchez-Monge Á. et al., 2014, *A&A*, 569, 11
- Sandell G., Goss W. M., Wright M., 2005, *ApJ*, 621, 839
- Shepherd D. S., Churchwell E., 1996, *ApJ*, 472, 225
- Shepherd D. S., Claussen M. J., Kurtz S. E., 2001, *Science*, 292, 1513
- Shu F. H., Adams F. C., Lizano S., 1987, *ARA&A*, 25, 23
- Smith R. J., Shetty R., Stutz A. M., Klessen R. S., 2012, *ApJ*, 750, 64
- Smith R. J., Shetty R., Beuther H., Klessen R. S., Bonnell I. A., 2013, *ApJ*, 771, 24
- Takami M., Karr J. L., Koh H., Chen H.-H., Lee H.-T., 2010, *ApJ*, 720, 155
- Turner J. L., Welch W. J., 1984, *ApJ*, 287, L81
- Wilner D. J., Welch W. J., Forster J. R., 1995, *ApJ*, 449, L73
- Wilner D. J., Reid M. J., Menten K. M., 1999, *ApJ*, 513, 755

- Wilson T. L., Johnston K. J., Mauersberger R., 1991, *A&A*, 251, 220
 Wilson T. L., Gaume R. A., Johnston K. J., 1993, *ApJ*, 402, 230
 Wink J. E., Duvert G., Guilloteau S., Gusten R., Walmsley C. M., Wilson T. L., 1994, *A&A*, 281, 505
 Wu J. W., Evans N. J., II, 2003, *ApJ*, 592, L79
 Wu Y., Wei Y., Zhao M., Shi Y., Yu W., Qin S., Huang M., 2004, *A&A*, 426, 503
 Wu Y., Zhu M., Wei Y., Xu D., Zhang Q., Fiege J. D., 2005, *ApJ*, 628, L57
 Wu Y. F., Henke S., Xue R., Guan X., Miller M., 2007, *ApJ*, 669, L37
 Wu Y. F., Qin S.-L., Guan X., Xue R., Ren Z., Liu T., Huang M., Chen S., 2009, *ApJ*, 697, L116
 Wu J. W., Evans N. J., II, Shirley Y. L., Knez C., 2010, *ApJS*, 188, 313
 Wyrowski F., Schilke P., Walmsley C. M., Menten K. M., 1999, *ApJ*, 514, L43
 Zapata L. A., Palau A., Ho P. T. P., Schilke P., Garrod R. T., Rodríguez L. F., Menten K., 2008, *A&A*, 479, L25
 Zapata L. A., Rodríguez-Garza C., Rodríguez L. F., Girart J. M., Chen H.-R., 2011, *ApJ*, 740, L19
 Zhang Q., Hunter T. R., Sridharan T. K., 1998, *ApJ*, 505, L151
 Zhang Q., Hunter T. R., Brand J., Sridharan T. K., Cesaroni R., Molinari S., Wang J., Kramer M., 2005, *ApJ*, 625, 864
 Zinnecker H., Yorke H. W., 2007, *ARA&A*, 45, 481

APPENDIX A: TWO-LAYER MODEL

The two-layer model (Myers et al. 1996; Di Francesco et al. 2001) is aimed at fitting the observed spectrum by setting the radiation temperatures of the continuum source J_c , the excitation temperature of the ‘rear’ and ‘front’ layers J_r and J_f , the cosmic background radiation J_b , the beam filling factor Φ , the systemic velocity V_{LSR} , the kinematic velocity V_k , the velocity dispersion σ , and the peak optical depth τ_0 . The predicted line brightness temperature at velocity V is given by

$$\begin{aligned} \Delta T_{\text{B}} = & (J_f - J_{\text{cr}})[1 - \exp(-\tau_f)] + (1 - \Phi) \\ & \times (J_r - J_b)[1 - \exp(-\tau_r - \tau_f)], \end{aligned} \quad (\text{A1})$$

where

$$J_{\text{cr}} = \Phi J_c + (1 - \Phi) J_r, \quad (\text{A2})$$

$$\tau_r = \tau_0 \exp\left[\frac{-(V - V_{\text{LSR}} - V_k)^2}{2\sigma^2}\right], \quad (\text{A3})$$

$$\tau_f = \tau_0 \exp\left[\frac{-(V - V_{\text{LSR}} + V_k)^2}{2\sigma^2}\right], \quad (\text{A4})$$

and the radiation temperature is expressed as $J_x = \frac{T_0}{\exp(T_0/T) - 1}$.

In this model the kinematic velocity is given by

$$V_k = \frac{\sigma^2}{V_R - V_B} \ln \frac{1 + \exp(T_{\text{BD}}/T_D)}{1 + \exp(T_{\text{RD}}/T_D)}, \quad (\text{A5})$$

where T_D is the brightness temperature of absorption dip, and T_{BD} and T_{RD} are the intensity of the blue and red peaks above the dip, respectively. Positive V_k corresponds to gas infalling on to the continuum core, while negative V_k indicates gas expansion (e.g. Myers et al. 1996; Aguti et al. 2007).

We applied the ‘lsqcurvefit’ method in MATLAB to fit the spectrum. We fitted the HCO^+ spectra first by setting all the parameters free. The line profile is mainly determined by V_{LSR} , σ , and V_k , while the intensity of the two peaks is mainly determined by τ_0 , Φ , J_c , J_f , and J_r . In the model, we set the ranges for τ_0 from 0.1 to 10, for the filling factor from 0 to 1, J_c , J_f , and J_r from 10 to 100 K, V_{LSR} from -50 to -43 km s^{-1} , σ from 0.1 to 3 km s^{-1} , V_k from 0.1 to 6 km s^{-1} . For each set of initial values, ‘lsqcurvefit’ will be converged to a solution and try to give the best estimated values. We find that τ_0 , Φ , J_c , J_f , and J_r are very sensitive to initial values and cannot be determined accurately due to degeneracy. Contrary to that, V_{LSR} , σ , and V_k are much less sensitive to the initial input values. When we change the initial values, the output for V_{LSR} , σ , and V_k only varies by less than 10 per cent. Thus, the error of the inferred infall speed is expected to be smaller than 10 per cent.

This paper has been typeset from a $\text{\TeX}/\text{\LaTeX}$ file prepared by the author.